Catchment landforms predict groundwater-dependent wetland sensitivity to recharge changes

Etienne Marti¹, Sarah Leray^{1,2}, Clément Roques³

- ¹ Departamento de Ingeniería Hidráulica y Ambiental, Pontificia Universidad Católica de Chile, Santiago, Chile
- ² Centro de Cambio Global UC, Santiago, Chile
- ³ Centre for Hydrogeology and Geothermics (CHYN), University of Neuchâtel, Neuchâtel, Switzerland

Correspondence to: Clément Roques (clement.roques@unine.ch)

Abstract. This study investigates the influence of topography on the desaturation rates of groundwater-dependent wetlands in response to changes in recharge. We examined sixty60 catchments across northern Chile, which feature a wide variety of landforms. We categorized the landforms_Landforms were categorized using geomorphon descriptors, identifying resulting in three distinct clusters: lowlandflat, transitionintermediatetransitional, and mountain settings. Using steady-state 3D groundwater models, we derived flow partitioning and seepage area extent for each catchment. Each cluster revealed exhibited consistent seepage areas evolution under varying wet-to-dry conditions. Our findings indicate that mountains exhibit have reduced seepage area compared to lowlands-flats at equivalent hydraulic conductivity to recharge (K/R) ratios, but are less sensitive to recharge fluctuations, with slower rates of seepage area wariationreduction. Statistical evidence demonstrates analyses show that geomorphons-defined landforms correlate with desaturation indicators, enabling the prediction of catchment sensitivity to climate change based solely on a topographic analysis-attributes.

Short summary. This studye research demonstrates shows that the response of groundwater-dependent wetlands to recharge changes can be accurately predicted solely based on from landform properties alone, providing a practical and scalable approach for wetland vulnerability assessment. We reveal that mMountain catchments are less sensitive to recharge changes than lowland flat eatchmentsones,— due to fewer but more persistent seepage areas. These results It offers critical insights for evaluating the support a scalable approach to assessing wetland vulnerability of eatchments to climate change, with practical implications—impacts and has direct implications—for water resource management and conservation planning inin diverse landscapes.

2.1. Introduction

<u>Changes in precipitation regimes and increasing temperatures driven by climate change are anticipated to significantly affect both surface and subsurface water resources</u> (Berghuijs et al., 2024; Konapala et al., 2020; Taylor et al., 2013). <u>Extended drought periods and reduced recharge are expected to threaten the functioning of groundwater-dependent ecosystems</u> (Kløve

et al., 2014; Rohde et al., 2024; Tetzlaff et al., 2024). These ecosystems rely on groundwater contributions to maintain their ecological structure and functional integrity, including processes that support biodiversity and key ecosystem services (Barron et al., 2014; Doody et al., 2017; Eamus & Froend, 2006). They encompass both terrestrial and aquatic environments, including wetlands, springs, rivers (riparian, aquatic, and hyporheic zones), lakes, grasslands, forests, as well as coastal and estuarine habitats (Eamus & Froend, 2006; Kløve et al., 2011). The extent to which groundwater-dependent ecosystems are vulnerable to climate-induced reductions in recharge depends not only on the hydrogeological properties of the underlying aquifer, but also on the role of landscape morphology in shaping groundwater flow and discharge patterns (Gleeson & Manning, 2008; Singha & Navarre-Sitchler, 2022). Identifying the physical controls on groundwater emergence at the land surface is therefore essential to improve our ability to anticipate groundwater-dependent ecosystems responses to climate variability.

distribution and temporal dynamics (Bresciani et al., 2014, 2016; Sophocleous, 2002). The interaction between groundwater and topography significantly impacts the resilience of groundwater-dependent wetlands to climate variability (Cuthbert et al., 2019; Scanlon et al., 2023). Considering steady-state groundwater flow systems, the depth of the water table, and so-the distribution of flow paths and groundwater seepage areas, are controlled by the groundwater recharge rate (*R*), the topography and by the hydrodynamic properties of the aquifer through its hydraulic conductivity (*K*), (Condon & Maxwell, 2015; Rath et al., 2023; Tóth, 1963; Zhang et al., 2022). An equivalence of effects between *R* and *K* has been demonstrated (Bresciani et al., 2014; Haitjema & Mitchell-Bruker, 2005; Jamieson & Freeze, 1982), allowing a convenient focus on the dimensionless $\frac{K}{R}$ ratio and the topography. In non-anthropized contexts, $\frac{K}{R}$ the groundwater table is typically near the surface in low-relief and/or humid regions, and deeper in rugged terrain and/or arid regions. However, the hydrogeological response and seepage dynamics to varying landscapes and topographic features are not straightforward and difficult to predict.

Analytical solutions have been proposed to quantify the extent of groundwater seepage under varying $\frac{K}{R}$ at the hillslope scale, using simplified groundwater flow equations (Bresciani et al., 2014, 2016). Marçais et al. (2017) conducted modeling experiments to estimate seepage extent and dynamics using a 2D representation of the equivalent hillslope. While these approaches are applicable in shallow aquifers, where flow predominantly follows the topography, they do not capture the complexity of 3D groundwater flow, especially under low water tables or steep reliefs. A few 3D numerical modeling experiments have been undertaken, mainly for sensitivity studies with conceptual surface and subsurface geometries (Carlier et al., 2019; Gauvain et al., 2021; Gleeson & Manning, 2008; Welch et al., 2012). There is a pressing need to better understand seepage-the distribution and dynamics of groundwater seepage, particularly in light of the complex considering the intricate topographic characteristics nuances of real-world conditions landscapes and the 3D nature of groundwater flow. This Such knowledge is essential critical for to-predicting the extent of groundwater seepage and the persistence of groundwater-its dependent wetlands under future climate scenarios.

To address this knowledge gap, we designed a numerical experiment to Our study aims to model the partitioning of 3D groundwater flows and the their seepage extent of seepage across different landscapes, from lowland-flat to high mountain

settings, considering various under varying $\frac{\kappa}{R}$ values. We applied this experiment on 60 catchments located in northern Chile, selected for their rich diversity of geomorphological contexts. Additionally, we aim to identify appropriate topographic indicators that explain the variety of hydrogeological responses and provide statistical means to extrapolate our findings to ungauged or data scarce regions. By linking geomorphologickey topographic patternscharacteristics of the catchments to groundwater seepage dynamics predicted by the model, we seekaim to improve the prediction of wetland desaturation risksensitivity under changing climate conditions. This approach supports the development of transferable frameworks for assessing the vulnerability of groundwater-dependent ecosystems vulnerability across heterogeneous terrain and provide statistical means to regionalize our findings, behaviors, providing statistical means to extrapolate our results to other contexts. We developed a parsimonious 3D groundwater flow modeling approach, which we applied to sixty60 catchments along 1,800 km of the northern Chile. This choice was motivated by the rich diversity of geomorphological contexts, allowing the exploration of a wide range of hydrogeological responses.

3.2. Material and Methods

65

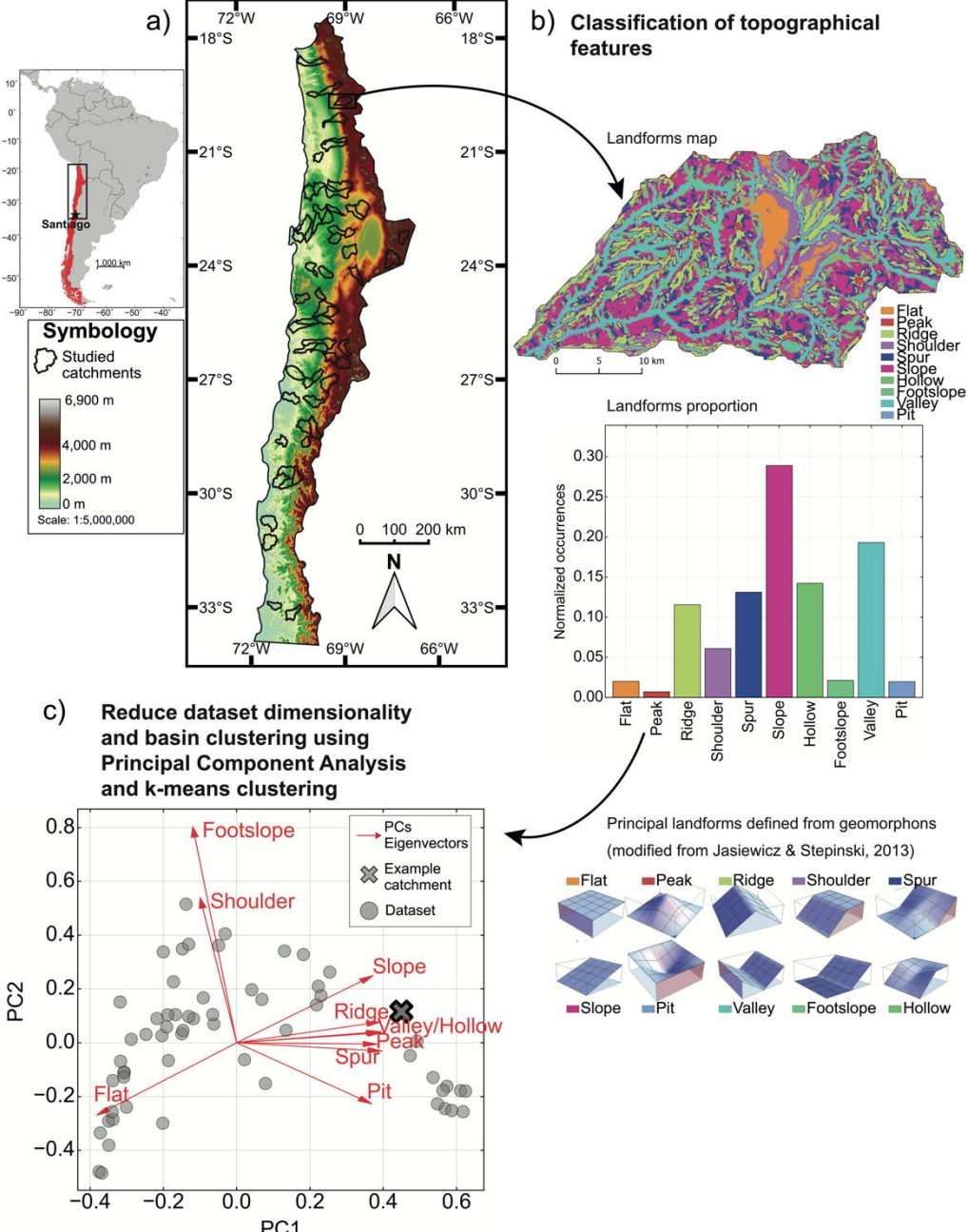
70

75

90

3.1.2.1. Geomorphological context

The study area is located in northern Chile between Santiago and the Peruvian border (-1,800 km long). The landforms diversity results from the specific tectonic and weathering processes involved in the Andes. This process resulted in the formation of a longitudinal valley called the Central Depression, which is bounded by two cordilleras, the Coastal Cordillera and the Principal Cordillera, both composed mainly of volcanic-sedimentary rocks (Hartley & Evenstar, 2010; Jordan et al., 1983). The Coastal Cordillera forms an intermediate mountain range with an average elevation between 1,000 and 2,000 m.a.s.l., while the Principal Andean Cordillera has maximum elevations close to 7,000 m.a.s.l. (Figure 1 Figure 1a) (Armijo et al., 2015; Charrier et al., 2007). The Central Depression delineates a sedimentary basin rich in Quaternary alluvial deposits with variable thicknesses, ranging from about 250 m near Santiago (Yáñez et al., 2015) to almost 1,000 m in the northern regions of Chile (Hartley & Evenstar, 2010; Jordan et al., 2014; Nester & Jordan, 2011). Specifically, the Pre-Cordillera is a transition zone between the Central Depression and the Western Cordillera, with catchment characteristics that vary from nearly flat terrain to mountainous regions with steep slope gradients and typical mountain front geomorphology (Figure 1 Figure 1a). The diversity of these environments provides an excellent opportunity to explore a wide range of topographic settings, including flat catchments, mountain-front areas, incised mountain catchments, volcanoes, and high mountain peaks.



area in northern Chile, with the boundaries of the 60 studied catchments highlighted in black. (b) Example of landform classification within a single catchment, including a landform map, the proportion of landform types, and an illustration of the principal landform categories defined by geomorphons (adapted from Jasiewicz & Stepinski, 2013). (c) Catchment categorization using Principal Component Analysis (PCA) for dimensionality reduction and clustering. The selected example catchment is plotted in the PCA space, illustrating its position relative to the first two principal components (PC1 and PC2) and to the whole dataset (grey dots). Red

3.2.2.2. Classification of catchment topographies

100

105

110

120

125

We considered the catchment boundaries of the global catchment database HydroATLAS (Lehner & Grill, 2013). We chose to limit the size of the catchments to between 500 and 1,500 km² by considering level 8 of HydroATLAS. To cover different geomorphological and tectonic settings, we selected sixty60 catchments within our study area (indicated by colored-black boundaries in Figure 1Figure 1a). We extracted the topography from the SRTM (Shuttle Radar Topography Mission, 90 m resolution) digital elevation model (DEM) from the SRTM (Shuttle Radar Topography Mission, 90 m resolution).

We used the geomorphons classification method proposed by Jasiewicz & Stepinski (2013) to categorize the topographies landform features within each catchments; e.g., flat, peak, ridge, shoulder, spur, slope, pit, valley, footslope, and hollow. into ten different landforms (Figure 1Figure 1b, note that). Ggeomorphons-defined landforms are italicized throughout the text for improved readability). This methodology is based on elevation differences in eight directions relative to the reference cell. This operation is reproduced for each cell of the DEM, identifying a shape for each of these cells (Figure 1Figure 1b). Unlike the direct cell neighbor method (e.g., slope, curvature, or roughness), the geomorphons method allows to capture for capturing landforms at larger scales by defining a search radius around the reference cell, the look-up distance in Jasiewicz & Stepinski (2013). Here we defined the search radiusit as a function of the equal to the -hillslope characteristic length:

$$L = \frac{1}{2D} \to L = \frac{1}{2*\frac{l}{4}},$$
 Equation (1)

where *L* is the catchment feature length, *l* is the river network length, *D* is the drainage density, and *A* is the catchment area. The river network is defined using a surface flow accumulation routine available in the Whitebox tool Python package (Lindsay, 2016). Combining principal component analysis (PCA) and k-means clustering methods (Figure 1Figure 1c), we categorized the catchments by their dominant topographical landform features based on landform proportions (Figure 1Figure 1b). PCA is a classical statistical method used to reduce the dataset dimensionality by transforming the original variables into a new set of uncorrelated variables, called principal components (PC), which capture the maximum variance in the data. The k-means clustering approach allows us to identify groups of catchments belonging to the cluster with the nearest mean within the new PC space (Figure 1Figure 1b and c). Here, we defined 3 main eategories clusters of catchments typical of flat, intermediate transitional, and mountain settings. Python code and trained models are available on the repository-(Marti et al., 2025)(Marti et al., 2024).

3.3.2.3. Numerical modelling of groundwater seepage areaextent

A three-dimensional numerical groundwater flow model was developed for each catchment. The models were constructed and run using the MODFLOW-2005 software suite (Harbaugh, 2005) with the NWT solver (Niswonger et al., 2011), and managed through the Python-based interface FLOPY (Bakker et al., 2016). The diffusivity equation was solved under steady-state conditions for unconfined flow.

The horizontal discretization followed the DEM resolution, set at 90 meters (Figure 2Figure 2a), while the vertical discretization consisted of ten layers with exponentially increasing thickness (Figure 2Figure 2b). To limit boundary effects. As buffer zone extending the modell domain by 20% around each catchment was added. expanded the modeled domain area by 20%, ensuring boundary A sensitivity analysis (Abhervé et al., 2023) of the extent of the buffer zone was performed to ensure that -conditions did not no impacts on the-seepage distribution was involved identified within the studied catchment (Figure 2Figure 2a). The model bottom mirrored the topography with a 100m-thick aquifer (Figure 2Figure 2b). Assuming a constant aguifer thickness minimized the potential effects of transmissivity changes on seepage distribution. The 100m thickness was chosen to realistically accommodate both flat sedimentary catchments and steep mountainous aguifers (Condon et al., 2020). The side and bottom boundaries of the buffer box were set as no-flow. For generality, effective recharge R was uniformly set at the water table across both the catchment and its buffer, enabling the simulation of both inflow and outflow across the model boundaries. This setup allowed considering interbassin groundwater exchanges, which are particularly likely to occur under low water table conditions that way particularly be involved at low water table elevation (Fan, 2019), and a A drain boundary condition (with a conductance equal to the product= of hydraulic conductivity with horizontal cell area K*dx*dy divided by the cell mid-thickness) was set on the topography using the eponymous packages in MODFLOW to allow exfiltration of groundwater wherever the water table rises to intersect the land surface. This method ensures that discharge occurs naturally along the topography, mimicking surface-connected wetlands and springs without imposing fixed fluxes or predefined discharge zones.

130

135

140

To solely focus on the effects of topography in the redistribution of groundwater seepage, we imposed homogeneous and isotropic hydraulic conductivity (K) across all modelled catchments. This simplification ensures that variability in seepage behavior arises solely from differences in landscape geometry and water table positions, rather than site-specific geological heterogeneity. Hydraulic conductivity (K) was set to be homogeneous and isotropic.

Various water table positions relative to the topography were derived by setting different values of the $\frac{K}{R}$ ratio, ranging from 100 for fully saturated conditions to 10,000 when all simulated catchments reached near full desaturation (i.e., when the normalized seepage area $S_A^* = \frac{seepage\ area}{catchment\ area} \frac{(S_A^*)}{(S_A^*)} < \frac{1\%}{R} \text{ reaches } \frac{1\%}{R}$ values were logarithmically spaced within this interval, and simulations were stopped if the catchment's seepage area fell below the 1% threshold (Figure 2Figure 2c). This allows us to consider a full range of conditions from humid to arid climates and low- to high-hydraulic conductivity settings. This modeling workflow resulted in a total of 1,793 simulations.

For each catchment, we perform a power law fit on the relationship between seepage area extent and $\frac{K}{R}$ further mentioned as the desaturation function ((2) Equation 2a, and red curve in Figure 2Figure 2Figure 2c). This allows us to capitalize on the observed linear relation between $\log (S_A^*)$ and $\log (\frac{K}{R})$:

$$S_A^* = \left(1 + \left(\frac{\frac{K}{R}}{\lambda}\right)^2\right)^n - \frac{\text{Equation (2a)}}{n}$$

$$\frac{dS_A^*}{d\frac{K}{R}} = \frac{2n}{\lambda^2} \frac{K}{R} \frac{S_A^*}{1 + \left(\frac{K}{R}\right)^2}$$
Equation (2b)

$$\frac{dS_A^*}{d\frac{K}{R}} \approx \frac{2nS_A^*}{\frac{K}{R}} \text{ when } \frac{K}{R} \gg \lambda$$
Equation (2c)

The desaturation function is determined by the proportionality constant, λ , which can be associated with a desaturation threshold, i.e., the critical value of $\frac{K}{R}$ above which the catchment begins to desaturate. The negative desaturation exponent, n, directly affects the rate of change in seepage extent as $\frac{K}{R}$ increases, as shown in Equations 2b and 2c. It can be viewed as a measure of the sensitivity of the seepage area extent to a deepening of the water table: for a given pair of seepage area and $\frac{K}{R}$, a lower n indicates a higher sensitivity of the catchment to a decrease of the water level. We estimated n considering seepage area extents lower than 20% of the catchment area, which are more representative of real-world conditions, i.e., by giving more weight in the fit to the higher $\frac{K}{R}$ ratios.

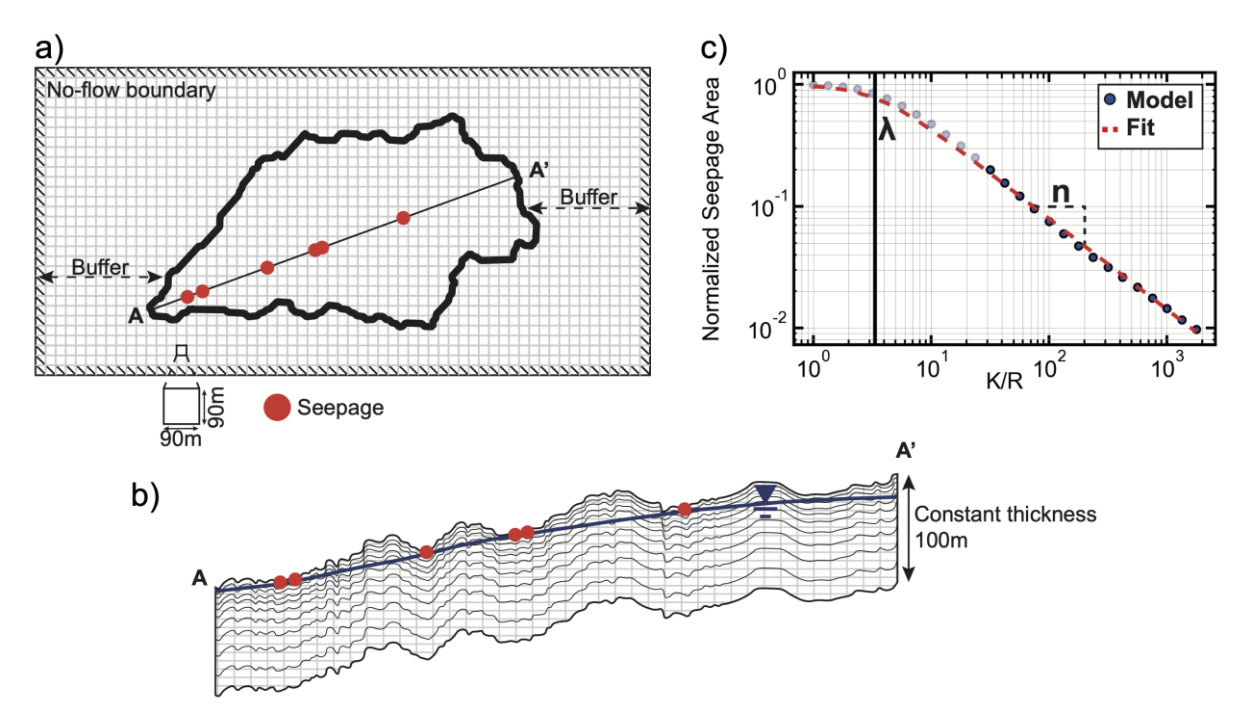


Figure 2: Model settings for one example catchment: (a) Horizontal discretization and buffer zone beyond catchment limits, (b) AA' cross-section including vertical discretization and an arbitrary water table intercepting the topography creating seepage areas (red dots), (c) Example of a-results of normalized seepage area with respect to K/R (grey and blue dots) with the power law fit for Eq. 2a (dashed red curve). The blue dots represent the normalized seepage area < 20% where the fit is-weighted is enhanced. TO BE COMPLETED!

2.4. Regionalization with Random Forest Random Forest methodalgorithm

To predict the desaturation response metrics λ and n from topographic descriptors and regionalize our findings, we employed Random Forest regression using the scikit-learn library in Python (Pedregosa et al., 2011). The input features for the model were the first two principal components (PC1 and PC2) derived from the sixty60 catchments. Random Forest models were trained independently for λ and n. Model performance and robustness were assessed using a bootstrap resampling procedure with 5,000 iterations. In each iteration, 10 catchments were randomly selected as a test set, while the remaining 50 were used for training. The coefficient of determination (R²) was calculated on the test data for each iteration, and the resulting R² distribution was used to evaluate model reliability (see Supplementary Material S2 for Kernel Density Estimate of R² values). Hyperparameter tuning for each model was performed using GridSearchCV with 2-fold cross-validation within each training subset. The tested parameter grid included n_estimators \in {50, 200, 500, 1000} and max_depth \in {None, 2, 10, 20}. The best combination of hyperparameters was used to retrain the model on the full training set in each iteration. The final Random Forest model was defined as the one achieving the best trade-off in predictive accuracy for both λ and n, and it was applied to

predict desaturation metrics in sixty630 three additional catchments located in South Chile. [@Etienne, please add detail on the methodology you use and move the supplementary material dedicated to this to the results as suggested by the reviewer]

We finally employed a Random Forest regression on the dataset to predict λ and n based on topographic parameters (PC1 and PC2) for sixty three catchments located both in the same study area and expanding further South inside Chile (Figure 4d and e). We defined PC1, PC2 and clusters for these new catchments using the originally trained PCA and k means model (Figure 4c). Regarding, training and testing of the Random Forest algorithm, we used the original sixty catchments dataset. This initial analysis involved 5,000 iterations of sampling with replacement, each using 10 test catchments, with the remaining 50 catchments used for training. This resampling approach was adopted to assess the robustness of the estimations in the presence of random variations within the selected test and training data and was evaluated calculating the coefficient of determination (R²) within the tested data (see Supplementary Material S2 for Kernel Density Estimate (KDE) plot of R² distribution). We defined the model used for predictions based on the best compromise to estimate both λ and n. Hyperparameters (number of trees and maximum depth) were tuned using cross validation techniques.

4.3. Results

185

190

195

200

205

210

4.1.3.1. Typology of catchments topography

We evaluate the proportion of main geomorphons on the sixty60-catchment dataset. The PCA analysis (Figure 1Figure 1-Figure 1-Figu

this cluster serves as a transition zone between flatter areas and mountain catchments, possibly including catchments showing both flat and mountainous characteristics, as observed at mountain fronts.

To facilitate comprehension and illustration, the <u>catchment eategories</u> se <u>clusters</u> are referred to as <u>lowland flat</u> <u>catchmenteluster</u> for the red cluster, <u>mountain eluster catchment</u> for the blue cluster, and <u>transitional</u> <u>eluster catchment</u> for the green cluster thereafter.

4.2.3.2. Seepage distribution evolution with increasing $\frac{K}{R}$

225

230

235

Figure 3Figure 3Figure 3a illustrates the evolution of seepage area, normalized by catchment area, as a function of $\frac{K}{R}$ for all sixty60 catchments. Four specific catchments are highlighted with sharper lines for further discussion. As expected, lower $\frac{K}{R}$ values result in fully saturated catchments, while as $\frac{K}{R}$ increases, all catchments progressively desaturate at varying rates. For instance, at a normalized seepage area of 20%, the corresponding $\frac{K}{R}$ values range from 20 to 250.

Similar to the distinct landform clusters, tThe desaturation behavior can be clearly differenciated for the of these 3 clusters categories clusters of catchments (Figure 3a) is clearly defined (Figure 1), confirming that variations in seepage distribution are predominantly driven by topographical effects. The power law fit of seepage distribution (Equation 3a) for each of the sixty60 catchments results in λ values ranging from 2.05 to 37.03 and n_1 values ranging from -0.44 to -0.31. The fit shows minimal RMSE values between 0.01 and 0.08, indicating that seepage evolution with increasing $\frac{K}{R}$ can be successfully parameterized with only two parameters, λ and n.

Regarding the desaturation threshold, λ , the mountain <u>cluster catchments</u> shows lower values than the <u>lowland-flat onescluster</u>. The transition<u>al catchments cluster demonstrates show intermediate</u> behavior, reaching higher λ values than the mountain <u>cluster catchments</u> but lower than the <u>lowland clusterflat ones</u>. Regarding the desaturation exponent, n, within the low-saturation domain ($\leq 20\%$), the mountain <u>cluster catchments</u> exhibits slower desaturation rates, while the <u>lowland clusterflats</u> presents faster desaturation rates. The variability in desaturation slopes for the transition<u>al catchments cluster</u> is more pronounced, reflecting a mix of behaviors within this zone, yet it again shows intermediate behavior relative to the other two clusters.

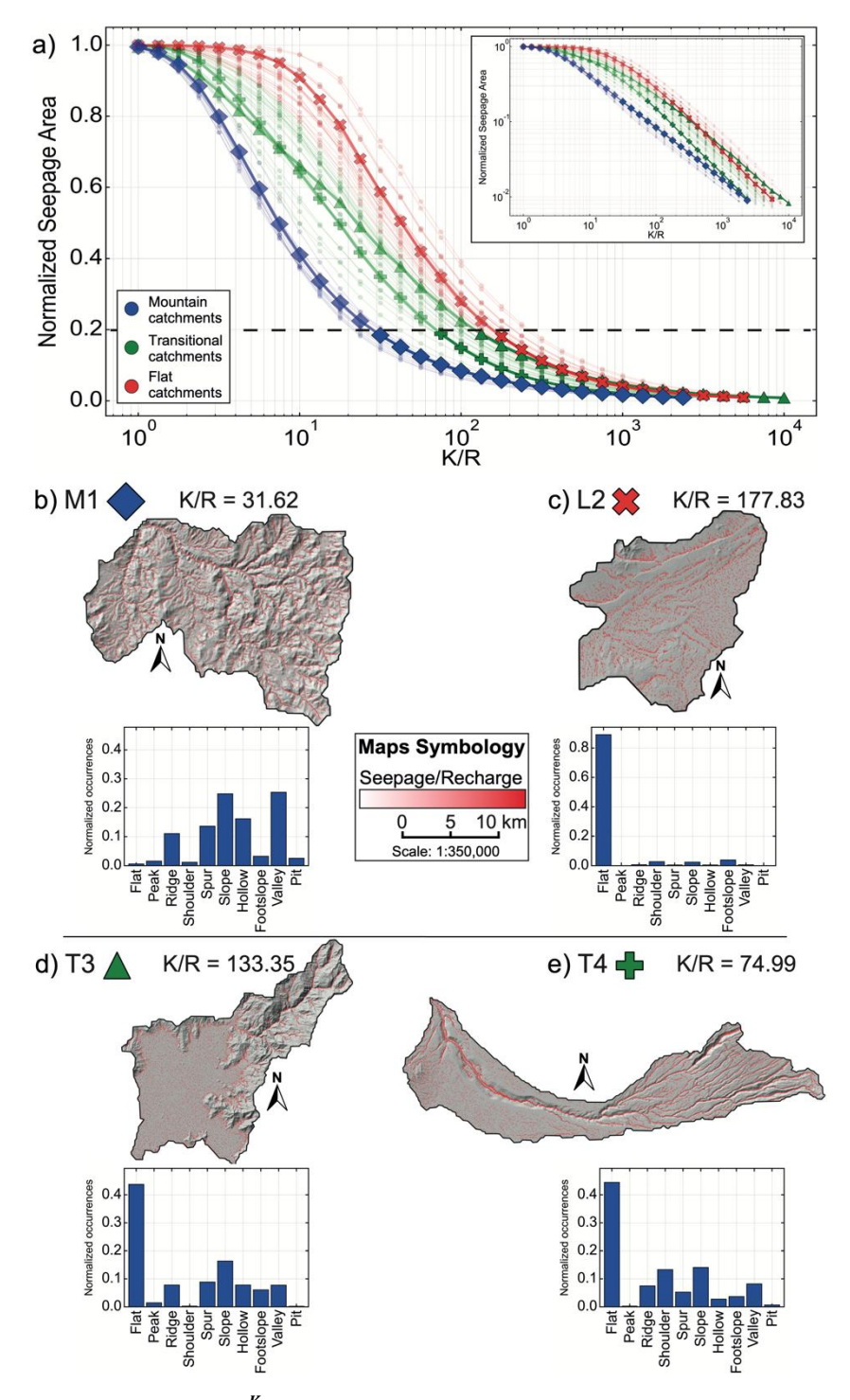


Figure 3: (a) Normalized seepage area against $\frac{K}{R}$ for the sixty60 catchments (colored lines with markers), including log-log plot on the upper-right corner. Four illustrative catchments are highlighted: mountain type M1 (blue diamond, (b)), lowland-flat type FL2 (red cross, (c)), transitory-transitional type T3 (green triangle, (d)) and T4 (green cross, (e)). Details include the topographic map

overlayed by the seepage $\frac{R}{R}$ value \frac{R} value $\frac{R}{R}$ value $\frac{R}{R}$ value $\frac{R}{R}$ value $\frac{R}{R$

4.3.3.3. Groundwater sSeepage patterns extent in four representative catchments

250

255

260

265

<u>Figure 3</u> Figure 3 highlights four distinct catchments: M1, representative of the mountain <u>cluster_catchments</u>; <u>FL</u>2, representing the <u>lowland_flat_cluster_catchments</u>; and T3 and T4, showing the range of responses within the <u>transitory_transitional catchmentscluster</u>. We present the seepage <u>over recharge</u> distribution over<u>layed on</u> the topographic map and the landform proportions for each catchment (Figure 3Figure 3b, c, d, and e).

For M1 (<u>Figure 3Figure 3</u>b), characterized by low λ and high n values, it exhibits the typical seepage distribution of mountainous regions. At a normalized area of 0.2, seepage primarily congregates in topographic lows, such as river valleys, while ridges and peaks desaturate due to their significant elevation compared to the surrounding terrain. Conversely, <u>FL2</u> (<u>Figure 3Figure 3</u>c), with high λ and low n values, suggests that the water table remains closer to the surface in <u>lowland-flat</u> settings.

_For T3 and T4, their landform proportions (<u>Figure 3</u>Figure 3d and e) reveal similar values for most forms, except for a higher proportion of *shoulder* and *footslope* forms in T4. This increased prevalence of *shoulder* landform in T4 is due to a prominent incised river valley in the eastern part of the catchment.

Examining T3's seepage distribution, it initially aligns with the mountain eluster-catchments with a low desaturation threshold (λ) . Then, in the range of $1 < \frac{K}{R} < 10$, a substantial change in the desaturation function slope is observed, with the distribution intersecting pattern converging toward the ones typical of that of the lowland clusterflat catchments for high $\frac{K}{R}$ values, ultimately being the last catchment to reach a saturation level of <1%. This behavior can be explained by looking at the spatial distribution of seepage for T3 (Figure 3Figure 3d). A clear demarcation contrast exists between the flat western area and the mountainous settings to the east. At higher elevations, desaturation occurs at lower $\frac{K}{R}$ values dominated by the steep landforms of the mountain settings and—, resulting in a low desaturation threshold (λ). Subsequently, at a normalized area of 0.2, the catchment behaves like the lowland cluster desaturation is mostly controlled by the western flat terrains, influenced by the western part of the catchment.

Conversely, T4's seepage distribution exhibits an opposite pattern. It initially mirrors the lowland-flat cluster with a higher λ value, ultimately resembling the mountain cluster characteristics, reaching saturation levels under 1% for similar $\frac{K}{R}$ values. The seepage spatial distribution for T4 (Figure 3Figure 3e) shows that flat landforms at higher elevation zones in the western part of the catchment have already undergone control the initiation of the desaturation and before being mostly controlled tend to develop exclusively within by the steep incised valley at lower elevations that tends to sustain the seepage extent. topographic lows, specifically at the bottom of the singular river channel.

4.4.3.4. Linking topographic features and desaturation behavior

270

275

We computed the correlation matrix between the principal components (PC1 and PC2) and the desaturation parameters (λ and n) to assess the strength of the topographical control on desaturation behavior. Figure 4Figure 4a shows a strong anti-correlation between λ and PC1, with a Spearman coefficient of r = -0.96 (p < 0.0001). Figure 4Figure 4b displays a strong linear correlation between n and PC1, with r = 0.76 (p < 0.0001). No other significant correlations were identified (the entire correlation matrix is available in Supplementary Material S1).

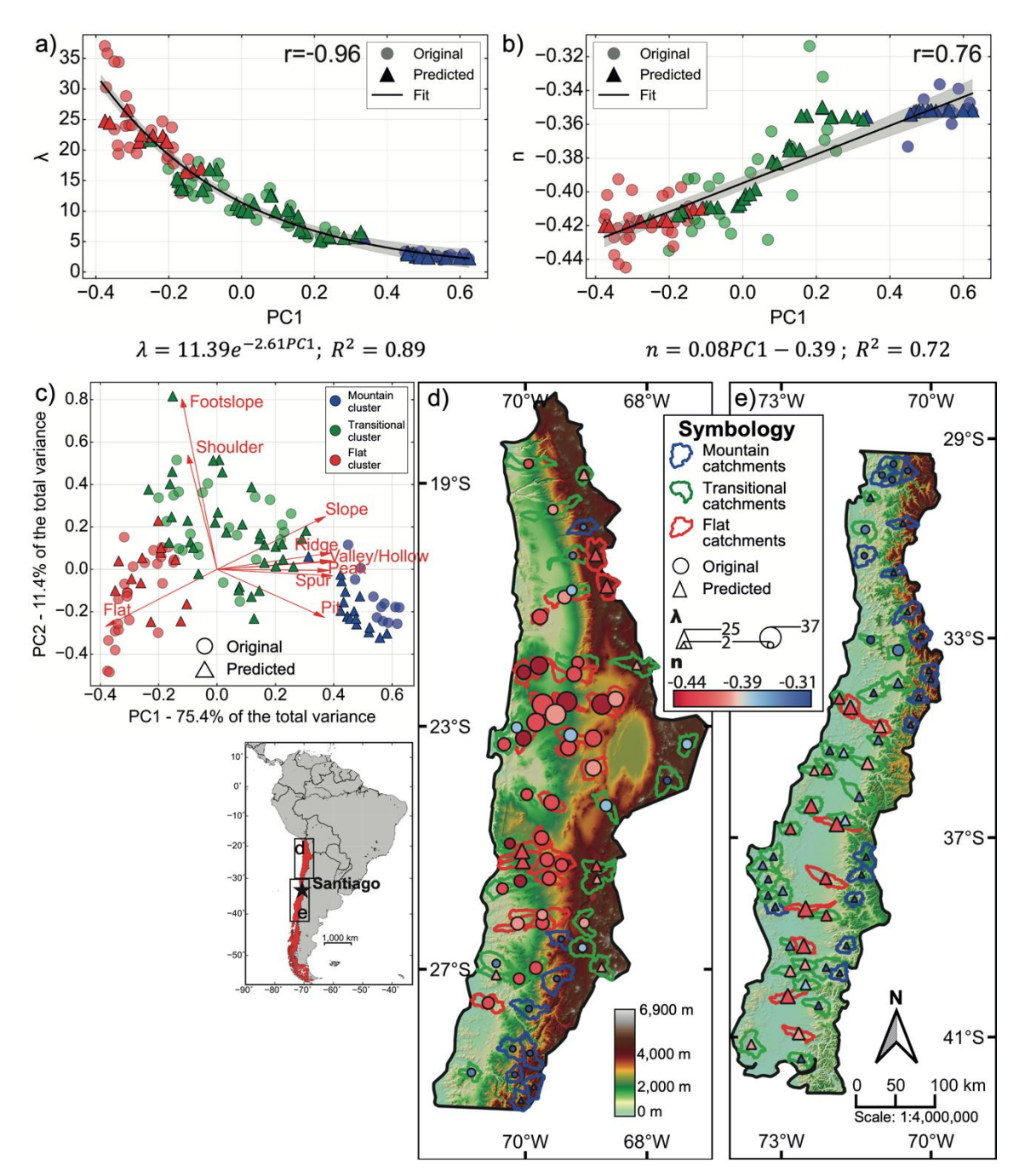


Figure 4: Scatter plots for the original sixty60-catchment dataset (dots) with Spearman coefficient r, the equation and the coefficient of determination (R^2) of a global fit (black line with 95% confidence interval) for (a) λ against PC1 and for (b) n against PC1. Random Forest predictions for both parameters are overlayed on the original data (erossestriangles). (c) PCA plot, for the original (dots) and the prediction (erossestriangles) datasets. The percentage of variance in the original dataset explained by each component is $\frac{displaiddisplayed}{displayed}$ on axis title. (d) and (e) Situation and topographic maps of the study area highlighting the $\frac{displaiddisplayed}{displayed}$ catchments with a colored according to the defined $\frac{displaiddisplayed}{displayed}$ catchments with a colored according to the defined $\frac{displaiddisplayed}{displayed}$ catchments with a colored according to the defined $\frac{displaiddisplayed}{displayed}$ catchments with a colored according to the defined $\frac{displaiddisplayed}{displayed}$

<u>mountain</u>). Each catchment is overlayed by a dot (original <u>dalaset dataset</u>) or a triangle (prediction dataset) <u>which whose</u> size depends on λ and the color for on n.

285

290

295

300

305

310

The <u>catchment categoriesclusters</u> elusters are well distinguishable in <u>Figure 4</u>Figure 4a and 4b. In <u>Figure 4</u>Figure 4a, the inverse relationship between λ and PC1 is robustly quantified by fitting an exponential function (R² = 0.89), facilitating a quantitative correlation between λ and PC1, as illustrated in <u>Figure 4</u>Figure 4a. The mountain cluster is isolated with a low average and variance in λ values. The transitional cluster forms the elbow part of the exponential decay, while the <u>lowland-flat</u> cluster is clearly identified with higher λ values. The variations in λ values are higher in the <u>lowland-flat</u> and transitional <u>clusters-catchments</u> compared to the mountain <u>clusterones</u>.

<u>Figure 4</u>Figure 4b reveals a linear relationship between n and PC1. The <u>excellent good linear fit</u> (R² = 0.72) allows for a straightforward quantification of the relationship between PC1 and the negative scaling exponent n and consequently, the appraisal of the desaturation rate based on landforms ((2Equations (2Equation 2)b and 2c). The <u>elusters catchment</u> categories clusters are well identified, with the <u>lowland flat</u> cluster showing lower n values than the mountain cluster.

We finally employed a Random Forest regression on the dataset to predict λ and n based on topographic parameters (PC1 and PC2) for sixty63 three catchments located both in the same study area and expanding further South inside Chile (Figure 4Figure 4d and 4e). We defined PC1, PC2, and clusters for these new catchments using the originally trained PCA and kmeans models (Figure 4Figure 4c). We finally employed a Random Forest regression on the dataset to predict λ and n based on topographic parameters (PC1 and PC2) for sixty three catchments located both in the same study area and expanding further South inside Chile (Figure 4d and e). We defined PC1, PC2 and clusters for these new eatehments using the originally trained PCA and k-means model (Figure 4e). Regarding, training and testing of the Random Forest algorithm, we used the original sixty eatehments dataset. This initial analysis involved 5,000 iterations of sampling with replacement, each using 10 test eatchments, with the remaining 50 catchments used for training. This resampling approach was adopted to assess the robustness of the estimations in the presence of random variations within the selected test and training data and was evaluated calculating the coefficient of determination (R²) within the tested data (see Supplementary Material S2 for Kernel Density Estimate (KDE) plot of $\mathbb{R}^{\frac{3}{2}}$ distribution). We defined the model used for predictions based on the best compromise to estimate both λ and n. Hyperparameters (number of trees and maximum depth) were tuned using cross-validation techniques. Predictions made for λ (Figure 4Figure 4a) show good consistency with the original dataset both in terms of identifying clusters behaviors and in trend, following the originally defined exponential relation. Regarding n (Figure 4Figure 4b), we observe a similar accuracy to represent clusters, while the general linear trend is less obvious. We observe for n, while following an increasing trend, diversified response between the clusters with the transitional eluster-catchments exhibiting a greater rate of change in n for an equivalent increment in PC1. Yet the it is a better fit to original data. The spatial distribution of the predicted catchments observed on Figure 4Figure 4d and 4e, is a good match with the original data, both in terms of topographic characteristics and desaturation function parameters.

5.4. Discussion and perspectives

315

320

325

340

345

Groundwater flow and storage regulate the resilience of wetlands to climate <u>variations</u>changes<u>variability</u> (Fan et al., 2019). Variations in topography and landforms across catchments lead to differences in wetland sensitivity to changing recharge by shaping distinct groundwater flow structures. In this study, we provide a quantitative assessment of the controls of landforms on the sensitivity of groundwater-dependent wetlands to aquifer desaturation (<u>expressed</u> through variations in the $\frac{K}{R}$ ratio <u>expressed</u> across a total of sixty one hundred and twenty three123-catchments along in Nothern Chile, covering spanning settings from lowlands flat to high mountains topographies. These feedback mechanisms were analyzed using a novel combination of three-dimensional process-based groundwater modeling, geomorphons-based landforms characterization classification, and multivariate statistical analysis, and Random Forest predictions at the regional scale.

Moreover, the proposed methodology demonstrated strong robustness to outliers and atypical landscape configurations. For exampleinstance, the Andes Mountains in northern Chile includeencompass the "Altiplano" region,— characterized bywhich features extensive flat areasterrains within an otherwise mountainous setting. The method successfully identified such catchments and classified them as *flat* (Figure 4Figure 4d between 19 and 23°S), illustrating its ability to reliably capture dominant landform characteristics eapacity to perform reliably across diverse geomorphological contexts.

Our results demonstrate that the desaturation functions of catchments can be explained by the typologies in topographives derived from landform categorization. Building on previous works that focused on two-dimensional aquifer geometry, as first introduced by Haitjema and Mitchell-Brucker (2005) and further explored by Bresciani et al. (2014), we show that mountainous regions exhibit lower seepage extents, restricted to incised valleys, compared to lowland-flat catchments at equivalent $\frac{K}{R}$ ratios. However, we demonstrate that mountainous regions are less sensitive to changes in saturation, exhibiting slower desaturation rates.

To disentangle the respective impacts of different landforms, we compared our results with those obtained from the analytical solution proposed by Bresciani et al. (2014) for a 1D hillslope, where one can easily assess the impacts of slope angle and the concavity/convexity of the hillslope (results in Supplementary Material S3). In agreement with our results, the steepness of the hillslope is the primary influence on seepage extent and its variation through changes in groundwater level. Steep slopes begin to desaturate at lower $\frac{K}{R}$ values than gentler slopes. Additionally, for a given change in groundwater level, the rate of change in seepage extent is inversely correlated with slope angle. This aligns with the differences in the desaturation exponent, n, and the desaturation threshold, λ , obtained for the mountain and lowland-flat clusters. Mountain clusters have higher n and λ values, suggesting higher resilience to changes in $\frac{K}{R}$.

Furthermore, the analysis of the simple analytical solution demonstrates that hillslope shape (concave vs. convex) also affects the desaturation function, though to a lesser extent than slope. Concave slopes appear to have a lower λ but a higher n than convex slopes. Similarities between concave and convex hillslopes can be found in the *shoulder* vs. *footslope* in our landform

classification. Shoulder and footslope is differentiated primarily along PC2, explaining a smaller proportion of the variance in the dataset analyzed here. However, no clear correlation between PC2, n, and λ was found, suggesting a minimal impact of shoulder and footslope landforms compared to the other ones.

While the aim of the present work is to establish a comprehensive exploration of landform controls on seepage dynamics, several simplifications limit its direct application to specific real-catchment systems. Although the models are based on real topographies from the Chilean Andes, the experiment does not intend to capture actual complexity of hydrogeological systems, but rather to explore a wide enough range of natural landform geometries for comparative analysis. First, we assumed homogeneous and isotropic aquifer properties with a fixed aquifer thickness, thereby neglecting geological heterogeneities, anisotropy, and variability in the depth of the active groundwater flow system (Frisbee et al., 2017; McIntosh & Ferguson, 2021), and consequently the seepage distribution, that can be involved in real landscape. While our use of the dimensionless that confers a robust approach for analyzing desaturation responses, future research could benefit from exploring additional parameters that account for catchment geometry, relief, or flow system depth. Additionally, the model results presented here operate under steady-state conditions and exclude the potential impacts of seasonal recharge variability, vegetation feedbacks, or the role of the unsaturated zone near the land surface. Exploring such processes, especially under transient conditions and with heterogeneous parameters, represents a promising perspective for future research.

6.5. Conclusion

350

355

360

365

370

375

To conclude, our study demonstrates that catchment-scale topographic features, quantified through geomorphon-based landform classification, exert a first-order control on groundwater seepage dynamics under varying recharge conditions. By linking these landforms to a desaturation functions, we show that the sensitivity of groundwater seepage extent to climate variability can be predicted from topography alone. This insight enables the development of a robust and scalable framework for assessing hydroclimatic vulnerability, particularly relevant for data-scarce regions. The ability to regionalize desaturation behavior using simple statistical learning tools, such as Random Forests as presented here, opens up new opportunities for applying this approach to ungauged basins in other regions (Hrachowitz et al., 2013). As such, our findings offer not only a methodological advance, but also enabledemonstrate potential for its application to assess the vulnerability of regional scale groundwater-dependent wetlands and the ecosystem they support to climate change.

Our results establish a robust statistical framework demonstrating a strong correlation between landforms, categorized by the dominant landforms (PC1), and hydrological parameters that assess the sensitivity of groundwater seepage to desaturation with changing recharge. This framework allows for predictions using straightforward statistical learning techniques. The Random Forest algorithm yields highly promising results for the sixty three catchments estimated. This approach provides valuable

insights into assessing eatchment vulnerability to climate change on a regional scale, even for ungauged basins (Hrachowitz et al., 2013).

380

390

Acknowledgments

We acknowledge funding from the Agencia Nacional de Investigación y Desarrollo (ANID) through grants Fondecyt Regular n°12510671210221, Anillo n°ATE220055, and Anillo n°ATE230006.

385 Open Research

The HydroATLAS global catchments database is freely available at https://www.hydrosheds.org/hydroatlas. The SRTM Digital Elevation model is available on NASA website (https://www.earthdata.nasa.gov/sensors/srtm). Python code to reproduce the analysis, the trained models (PCA, k-means and Random Forest), and the data used to generate results and figures in this manuscript is publicly available at Marti et al-_(2025)(2024). This includes landfoms proportion, PCA, cluster information, λ and n values, and seepage area distribution for each catchment of the original dataset. The predicted dataset is also included (PCA, clusters, λ and n estimations). Catchments ID correspond to the HydroATLAS identification.

Competing interests

The contact author has declared that none of the authors has any competing interests.

395 References

- Abhervé, R., Roques, C., Gauvain, A., Longuevergne, L., Louaisil, S., Aquilina, L., & De Dreuzy, J.-R. (2023). Calibration of groundwater seepage against the spatial distribution of the stream network to assess catchment-scale hydraulic properties. *Hydrology and Earth System Sciences*, 27(17), 3221–3239. https://doi.org/10.5194/hess-27-3221-2023
- Armijo, R., Lacassin, R., Coudurier-Curveur, A., & Carrizo, D. (2015). Coupled tectonic evolution of Andean orogeny and global climate. *Earth-Science Reviews*, *143*, 1–35. https://doi.org/10.1016/j.earscirev.2015.01.005
 - Bakker, M., Post, V., Langevin, C. D., Hughes, J. D., White, J. T., Starn, J. J., & Fienen, M. N. (2016). Scripting MODFLOW Model Development Using Python and FloPy. *Groundwater*, *54*(5), 733–739. https://doi.org/10.1111/gwat.12413
 - Barron, O. V., Emelyanova, I., Van Niel, T. G., Pollock, D., & Hodgson, G. (2014). Mapping groundwater-dependent ecosystems using remote sensing measures of vegetation and moisture dynamics: GDES MAPPING USING REMOTE
- 405 MEASURES OF VEGETATION/MOISTURE DYNAMICS. *Hydrological Processes*, 28(2), 372–385. https://doi.org/10.1002/hyp.9609
 - Berghuijs, W. R., Collenteur, R. A., Jasechko, S., Jaramillo, F., Luijendijk, E., Moeck, C., Van Der Velde, Y., & Allen, S. T. (2024). Groundwater recharge is sensitive to changing long-term aridity. *Nature Climate Change*, *14*(4), 357–363. https://doi.org/10.1038/s41558-024-01953-z
- Bresciani, E., Davy, P., & de Dreuzy, J.-R. (2014). Is the Dupuit assumption suitable for predicting the groundwater seepage area in hillslopes? *Water Resources Research*, 50(3), 2394–2406. https://doi.org/10.1002/2013WR014284

 Bresciani, E., Coderniaux, P. & Batelaan, O. (2016). Hydrogeological controls of water table-land surface interactions: Water
 - Bresciani, E., Goderniaux, P., & Batelaan, O. (2016). Hydrogeological controls of water table-land surface interactions: Water Table-Land Surface Interactions. *Geophysical Research Letters*, 43(18), 9653–9661. https://doi.org/10.1002/2016GL070618 Carlier, C., Wirth, S. B., Cochand, F., Hunkeler, D., & Brunner, P. (2019). Exploring Geological and Topographical Controls

- on Low Flows with Hydrogeological Models. *Groundwater*, *57*(1), 48–62. https://doi.org/10.1111/gwat.12845 Charrier, R., Pinto, L., & Rodríguez, M. P. (2007). Tectonostratigraphic evolution of the Andean Orogen in Chile. In T. Moreno & W. Gibbons (Eds.), *The Geology of Chile* (First, pp. 21–114). The Geological Society of London. https://doi.org/10.1144/GOCH.3
- Bottom of a Watershed? *Water Resources Research*, 56(3), e2019WR026010. https://doi.org/10.1029/2019WR026010 Condon, L. E., & Maxwell, R. M. (2015). Evaluating the relationship between topography and groundwater using outputs from a continental-scale integrated hydrology model. *Water Resources Research*, 51(8), 6602–6621. https://doi.org/10.1002/2014WR016774

Condon, L. E., Markovich, K. H., Kelleher, C. A., McDonnell, J. J., Ferguson, G., & McIntosh, J. C. (2020). Where Is the

- Cuthbert, M. O., Gleeson, T., Moosdorf, N., Befus, K. M., Schneider, A., Hartmann, J., & Lehner, B. (2019). Global patterns and dynamics of climate–groundwater interactions. *Nature Climate Change*, 9(2), 137–141. https://doi.org/10.1038/s41558-018-0386-4
 - Doody, T. M., Barron, O. V., Dowsley, K., Emelyanova, I., Fawcett, J., Overton, I. C., Pritchard, J. L., Van Dijk, A. I. J. M., & Warren, G. (2017). Continental mapping of groundwater dependent ecosystems: A methodological framework to integrate diverse data and expert opinion. *Journal of Hydrology: Regional Studies*, 10, 61–81. https://doi.org/10.1016/j.ejrh.2017.01.003
- Eamus, D., & Froend, R. (2006). Groundwater-dependent ecosystems: The where, what and why of GDEs. *Australian Journal of Botany*, *54*(2), 91. https://doi.org/10.1071/BT06029
 Fan, Y. (2019). Are catchments leaky? *WIREs Water*, *6*(6). https://doi.org/10.1002/wat2.1386
 - Fan, Y. (2019). Are catchments leaky? *WIREs Water*, 6(6). https://doi.org/10.1002/wat2.1386
 - Fan, Y., Clark, M., Lawrence, D. M., Swenson, S., Band, L. E., Brantley, S. L., Brooks, P. D., Dietrich, W. E., Flores, A., Grant, G., Kirchner, J. W., Mackay, D. S., McDonnell, J. J., Milly, P. C. D., Sullivan, P. L., Tague, C., Ajami, H., Chaney, N.,
- Hartmann, A., ... Yamazaki, D. (2019). Hillslope Hydrology in Global Change Research and Earth System Modeling. Water Resources Research, 55(2), 1737–1772. https://doi.org/10.1029/2018WR023903
 Frisbee, M. D., Tolley, D. G., & Wilson, J. L. (2017). Field estimates of groundwater circulation depths in two mountainous watersheds in the western U.S. and the effect of deep circulation on solute concentrations in streamflow. Water Resources Research, 53(4), 2693–2715. https://doi.org/10.1002/2016WR019553
- Gauvain, A., Leray, S., Marçais, J., Roques, C., Vautier, C., Gresselin, F., Aquilina, L., & Dreuzy, J. (2021). Geomorphological Controls on Groundwater Transit Times: A Synthetic Analysis at the Hillslope Scale. *Water Resources Research*, *57*(7). https://doi.org/10.1029/2020WR029463
 Gleeson, T., & Manning, A. H. (2008). Regional groundwater flow in mountainous terrain: Three-dimensional simulations of
- Haitjema, H. M., & Mitchell-Bruker, S. (2005). Are Water Tables a Subdued Replica of the Topography? *Groundwater*, 43(6), 781–786. https://doi.org/10.1111/j.1745-6584.2005.00090.x Harbaugh, A. W. (2005). *MODFLOW-2005: The U.S. Geological Survey modular ground-water model—The ground-water*

topographic and hydrogeologic controls. Water Resources Research, 44(10). https://doi.org/10.1029/2008WR006848

flow process (Report 6-A16; Techniques and Methods). USGS Publications Warehouse. https://doi.org/10.3133/tm6A16

- Hartley, A. J., & Evenstar, L. (2010). Cenozoic stratigraphic development in the north Chilean forearc: Implications for basin development and uplift history of the Central Andean margin. *Tectonophysics*, 495(1–2), 67–77. https://doi.org/10.1016/j.tecto.2009.05.013
 - Hrachowitz, M., Savenije, H. H. G., Blöschl, G., McDonnell, J. J., Sivapalan, M., Pomeroy, J. W., Arheimer, B., Blume, T., Clark, M. P., Ehret, U., Fenicia, F., Freer, J. E., Gelfan, A., Gupta, H. V., Hughes, D. A., Hut, R. W., Montanari, A., Pande, S., Tetzlaff, D., ... Cudennec, C. (2013). A decade of Predictions in Ungauged Basins (PUB)—A review. *Hydrological*
- 455 Sciences Journal, 58(6), 1198–1255. https://doi.org/10.1080/02626667.2013.803183
 Jamieson, G. R., & Freeze, R. A. (1982). Determining Hydraulic Conductivity Distributions in a Mountainous Area Using Mathematical Modeling. Ground Water, 20(2), 168–177. https://doi.org/10.1111/j.1745-6584.1982.tb02745.x
 Jasiewicz, J., & Stepinski, T. F. (2013). Geomorphons—A pattern recognition approach to classification and mapping of landforms. Geomorphology, 182, 147–156. https://doi.org/10.1016/j.geomorph.2012.11.005
- Jordan, T. E., Isacks, B. L., Allmendinger, R. W., Brewer, J. A., Ramos, V. A., & Ando, C. J. (1983). Andean tectonics related to geometry of subducted Nazca plate. *Geological Society of America Bulletin*, 94(3), 341. https://doi.org/10.1130/0016-7606(1983)94<341:ATRTGO>2.0.CO;2
 - Jordan, T. E., Kirk-Lawlor, N. E., Blanco, N. P., Rech, J. A., & Cosentino, N. J. (2014). Landscape modification in response to repeated onset of hyperarid paleoclimate states since 14 Ma, Atacama Desert, Chile. *Geological Society of America Bulletin*,

- 465 126(7–8), 1016–1046. https://doi.org/10.1130/B30978.1 Kløve, B., Ala-aho, P., Bertrand, G., Boukalova, Z., Ertürk, A., Goldscheider, N., Ilmonen, J., Karakaya, N., Kupfersberger, H., Kværner, J., Lundberg, A., Mileusnić, M., Moszczynska, A., Muotka, T., Preda, E., Rossi, P., Siergieiev, D., Šimek, J., Wachniew, P., ... Widerlund, A. (2011). Groundwater dependent ecosystems. Part I: Hydroecological status and trends. Environmental Science & Policy, 14(7), 770–781. https://doi.org/10.1016/j.envsci.2011.04.002
- Kløve, B., Ala-Aho, P., Bertrand, G., Gurdak, J. J., Kupfersberger, H., Kværner, J., Muotka, T., Mykrä, H., Preda, E., Rossi, P., Uvo, C. B., Velasco, E., & Pulido-Velazquez, M. (2014). Climate change impacts on groundwater and dependent ecosystems. *Journal of Hydrology*, 518, 250–266. https://doi.org/10.1016/j.jhydrol.2013.06.037
 Konapala, G., Mishra, A. K., Wada, Y., & Mann, M. E. (2020). Climate change will affect global water availability through compounding changes in seasonal precipitation and evaporation. *Nature Communications*, 11(1), 3044.
- https://doi.org/10.1038/s41467-020-16757-w
 Lehner, B., & Grill, G. (2013). Global river hydrography and network routing: Baseline data and new approaches to study the world's large river systems. *Hydrological Processes*, 27(15), 2171–2186. https://doi.org/10.1002/hyp.9740
 Lindsay, J. B. (2016). Whitebox GAT: A case study in geomorphometric analysis. *Computers & Geosciences*, 95, 75–84. https://doi.org/10.1016/j.cageo.2016.07.003
- 480 Marçais, J., De Dreuzy, J.-R., & Erhel, J. (2017). Dynamic coupling of subsurface and seepage flows solved within a regularized partition formulation. Advances in Water Resources, 109, 94–105. https://doi.org/10.1016/j.advwatres.2017.09.008
 Marti, E., Leray, S., & Roques, C. (2025). Dataset used in "Catchment landforms predict groundwater-dependent wetland
 - Marti, E., Leray, S., & Roques, C. (2025). Dataset used in "Catchment landforms predict groundwater-dependent wetland sensitivity to recharge changes", manuscript submitted to HESS. [Dataset]. Zenodo.
- 485 https://doi.org/10.5281/ZENODO.10144981
 - McIntosh, J. C., & Ferguson, G. (2021). Deep Meteoric Water Circulation in Earth's Crust. *Geophysical Research Letters*, 48(5), e2020GL090461. https://doi.org/10.1029/2020GL090461
 - Nester, P., & Jordan, T. (2011). The Pampa del Tamarugal Forearc Basin in Northern Chile: The Interaction of Tectonics and Climate. In C. Busby & A. Azor (Eds.), *Tectonics of Sedimentary Basins* (1st ed., pp. 369–381). Wiley.
- https://doi.org/10.1002/9781444347166.ch18
 Niswonger, R. G., Panday, S., & Ibaraki, M. (2011). MODFLOW-NWT, a Newton formulation for MODFLOW-2005 (Report 6-A37; Techniques and Methods). USGS Publications Warehouse. https://doi.org/10.3133/tm6A37
 Pedregosa, F., Varoquaux, G., Gramfort, A., Michel, V., Thirion, B., Grisel, O., Blondel, M., Prettenhofer, P., Weiss, R., Dubourg, V., Vanderplas, J., Passos, A., Cournapeau, D., Brucher, M., Perrot, M., & Duchesnay, É. (2011). Scikit-learn:
- 495 Machine Learning in Python. *Journal of Machine Learning Research*, *12*(85), 2825–2830.

 Rath, P., Bresciani, E., Zhu, J., & Befus, K. M. (2023). Numerical analysis of seepage faces and subaerial groundwater discharge near waterbodies and on uplands. *Environmental Modelling & Software*, *169*, 105828. https://doi.org/10.1016/j.envsoft.2023.105828
- Rohde, M. M., Albano, C. M., Huggins, X., Klausmeyer, K. R., Morton, C., Sharman, A., Zaveri, E., Saito, L., Freed, Z., Howard, J. K., Job, N., Richter, H., Toderich, K., Rodella, A.-S., Gleeson, T., Huntington, J., Chandanpurkar, H. A., Purdy, A. J., Famiglietti, J. S., ... Stella, J. C. (2024). Groundwater-dependent ecosystem map exposes global dryland protection needs. *Nature*, *632*(8023), 101–107. https://doi.org/10.1038/s41586-024-07702-8
 - Scanlon, B. R., Fakhreddine, S., Rateb, A., De Graaf, I., Famiglietti, J., Gleeson, T., Grafton, R. Q., Jobbagy, E., Kebede, S., Kolusu, S. R., Konikow, L. F., Long, D., Mekonnen, M., Schmied, H. M., Mukherjee, A., MacDonald, A., Reedy, R. C.,
- 505 Shamsudduha, M., Simmons, C. T., ... Zheng, C. (2023). Global water resources and the role of groundwater in a resilient water future. *Nature Reviews Earth & Environment*, 4(2), 87–101. https://doi.org/10.1038/s43017-022-00378-6 Singha, K., & Navarre-Sitchler, A. (2022). The Importance of Groundwater in Critical Zone Science. *Groundwater*, 60(1), 27–34. https://doi.org/10.1111/gwat.13143
- Sophocleous, M. (2002). Interactions between groundwater and surface water: The state of the science. *Hydrogeology Journal*, 10(1), 52–67. https://doi.org/10.1007/s10040-001-0170-8
 - Taylor, R. G., Scanlon, B., Döll, P., Rodell, M., van Beek, R., Wada, Y., Longuevergne, L., Leblanc, M., Famiglietti, J. S., Edmunds, M., Konikow, L., Green, T. R., Chen, J., Taniguchi, M., Bierkens, M. F. P., MacDonald, A., Fan, Y., Maxwell, R. M., Yechieli, Y., ... Treidel, H. (2013). Ground water and climate change. *Nature Climate Change*, *3*(4), 322–329. https://doi.org/10.1038/nclimate1744

- 515 Tetzlaff, D., Laudon, H., Luo, S., & Soulsby, C. (2024). Ecohydrological resilience and the landscape water storage continuum in droughts. *Nature Water*, 2(10), 915–918. https://doi.org/10.1038/s44221-024-00300-y

 Tóth, J. (1963). A theoretical analysis of groundwater flow in small drainage basins. *Journal of Geophysical Research*, 68(16),
 - 4795–4812. https://doi.org/10.1029/JZ068i016p04795
- Welch, L. A., Allen, D. M., & Van Meerveld, H. J. (2012). Topographic Controls on Deep Groundwater Contributions to
 520 Mountain Headwater Streams and Sensitivity to Available Recharge. *Canadian Water Resources Journal / Revue Canadienne Des Ressources Hydriques*, 37(4), 349–371. https://doi.org/10.4296/cwrj2011-907
 - Yáñez, G., Munoz, M., Flores-Aqueveque, V., & Bosch, A. (2015). Gravity derived depth to basement in Santiago Basin, Chile: Implications for its geological evolution, hydrogeology, low enthalpy geothermal, soil characterization and geo-hazards. *Andean Geology*, 42(2), 147–172. https://doi.org/10.5027/andgeoV42n2-a01
- 525 Zhang, X., Jiao, J. J., & Guo, W. (2022). How Does Topography Control Topography-Driven Groundwater Flow? *Geophysical Research Letters*, 49(20), e2022GL101005. https://doi.org/10.1029/2022GL101005